

RADIOFREQUENCY FIELD INHOMOGENEITY COMPENSATION IN HIGH SPATIAL RESOLUTION MAGNETIC RESONANCE SPECTROSCOPIC IMAGING

ALESSANDRO PASSERI*, STEFANO MAZZUCA†, AND VERONICA DEL BENE‡

Abstract. Clinical magnetic resonance spectroscopy imaging (MRSI) is a non-invasive functional technique, whose mathematical framework falls into the category of linear inverse problems. However, its use in medical diagnostics is hampered by two main problems, both linked to the Fourier-based technique usually implemented for spectra reconstruction: poor spatial resolution and severe blurring in spatial localization of the reconstructed spectra. Moreover, the intrinsic *ill-posedness* of the MRSI problem might be worsened by *i*) spatially dependent distortions of the static magnetic field (B_0) distribution, as well as by *ii*) inhomogeneity in the power deposition distribution of the radiofrequency magnetic field (B_1). Among several alternative methods, SLIM (Spectral Localization by IMaging) and BSLIM (B_0 compensated SLIM) are reconstruction algorithms in which *a priori* information concerning the spectroscopic target is introduced into the reconstruction kernel. Nonetheless, the influence of the B_1 field, particularly when its operating wavelength is close to the size of the human organs being studied, continues to be disregarded. *starSLIM* (STatic and Radiofrequency-compensated SLIM), an evolution of the SLIM and BSLIM methods, is therefore proposed, in which the transformation kernel also includes the B_1 field inhomogeneity map, thus allowing almost complete 3D modelling of the MRSI problem. Moreover, an original method for experimental determination of the B_1 field inhomogeneity map specific to the target under evaluation is also included. The compensation capabilities of the proposed method have been tested and illustrated using synthetic raw data reproducing the human brain.

1. Introduction. Tomographic imaging of *in vivo* biological tissues, [1] is a technique that, from a mathematical perspective, falls into the category of linear inverse problems, whose field of application embraces a broad spectrum of imaging techniques.

In accordance with a known concept in numerical analysis applied to imaging when inverse problems are involved, physical information concerning the acquisition process, as well as information describing the geometry of the acquisition system, form the numerical structure of the linear operator that represents the mathematical model of the instrumentation involved into the experimental process [2] [3]. In particular, if $f^{(0)}$ and g are elements of separable L^2 -Hilbert spaces \mathcal{X} and \mathcal{Y} [4], respectively, then the imaging process may be described by a linear mapping

$$g = Af^{(0)} + w \quad (1.1)$$

where g is the noisy image of the object $f^{(0)}$ and A is the transition matrix from the object space \mathcal{X} into the image space \mathcal{Y} . In the above equation, w is an element of the \mathcal{Y} space representing the noise component of the g image.

As is usual, the experimental image g may be described by a finite set of scalar values representing both the spatial and the temporal response of a biological structure investigated under different measurement conditions [5] [6]. Denoting this set by g_1, g_2, \dots, g_M , an image can be viewed as a vector too, denoted by \mathbf{g} , whose components g_m are proportional to the sampled values of the continuous image g

$$g_m = g(\mathbf{x}_m); \quad m = 1, 2, \dots, M \quad (1.2)$$

*Biomolecular Nuclear Medicine, University of Florence, Florence, Italy.

†Biomolecular Nuclear Medicine, University of Florence, Florence, Italy.

‡CIRM: Interdepartmental Center for Research in Nuclear Magnetic Resonance, University of Florence, Florence, Italy.

where the proportionality constant has, for simplicity, been omitted and \mathbf{x}_m is the vector of parameters identifying the m^{th} measurement condition.

Moreover, if we use $p_m(\mathbf{x})$ to denote the response function, associated with the detecting instrument, evaluated at the m^{th} condition, g_m may be better represented by the weighted averages of g :

$$g_m = \int p_m(\mathbf{x})g(\mathbf{x})d\mathbf{x} \quad (1.3)$$

thus defining the scalar product $g_m = (g, p_m)_{\mathcal{Y}}$ between the response functions $p_m(\mathbf{x})$ and g , the subscript \mathcal{Y} indicating the space where the scalar product is defined.

The instrumental response in the object space may be represented by basis functions directly related to the integral kernel of the imaging operator

$$\varphi_m(\mathbf{x}') = (A^*p_m)(\mathbf{x}'); \quad m = 1, 2, \dots, M \quad (1.4)$$

where A^* is the adjoint of the operator A , such that

$$g_m^{(0)} = (Af^{(0)}, p_m)_{\mathcal{Y}} = (f^{(0)}, A^*p_m)_{\mathcal{X}} = (f^{(0)}, \varphi_m)_{\mathcal{X}} \quad (1.5)$$

The above equation may be restated as

$$g_m^{(0)} = \int_{\mathcal{D}} \varphi_m(\mathbf{x}')f^{(0)}(\mathbf{x}')d\mathbf{x}' \quad (1.6)$$

where \mathcal{D} is the object domain; thus, the components of the noise-free discrete image behave as generalized moments of $f^{(0)}$.

Physical information concerning the imaging problem under study, as well as the instrumental response behaviour under specific acquisition conditions, are represented by the basis functions $\varphi_m(\mathbf{x}')$, whose accurate characterization is necessary in order to reduce the intrinsic loss of stability of the solution related to the ill-conditioned nature of the imaging problem [7] [8].

Clinical magnetic resonance spectroscopy imaging (MRSI) is a non-invasive functional imaging technique, whose mathematical framework is very similar to the one briefly outlined above [9] [10]. In fact, as approached by the conventional and widely used chemical shift imaging (CSI) method [11] [12] [13], the MRSI signal $r(\mathbf{k}, t)$ obtained from a phase-encoding experiment performed in a uniform magnetic field, may usually be written as

$$r(\mathbf{k}, t) = \int_{-\infty}^{\infty} \int_{\mathcal{D}} \rho(\mathbf{x}, \omega) e^{-i2\pi(\mathbf{k}\mathbf{x} + \omega t)} d\mathbf{x} d\omega \quad (1.7)$$

where $\rho(\mathbf{x}, \omega)$ represents the spatially variable spectral information in the object space, $\mathbf{k} \equiv (k_x, k_y, k_z)$ is the three-dimensional phase encoding wave vector, \mathbf{x} is the three-dimensional spatial coordinate vector and ω is the temporal frequency. In this case, the basis functions φ_m , introduced by eq.(1.4), are represented by the elementary harmonics $e^{-i2\pi(\mathbf{k}\mathbf{x} + \omega t)}$, where neither information regarding the biological system under examination, nor information concerning the physical characteristics of the acquisition instrumentation can be found. This is the main reason for the inadequacy of the CSI method to tackle the MRSI problem [14].

Moreover, since only a finite set of signals can be acquired, available at the $\mathbf{k}_{n_k} =$

$n_k \Delta \mathbf{k}$ and $t_{n_t} = n_t \Delta t$ sampling points in the four-dimensional object space, the CSI method finds an approximate solution $\tilde{\rho}(\mathbf{x}, \omega)$ to eq.(1.7), namely

$$\tilde{\rho}(\mathbf{x}, \omega) = \sum_{n_k} \sum_{n_t} r(\mathbf{k}_{n_k}, n_t \Delta t) e^{i2\pi(\mathbf{k}_{n_k} \cdot \mathbf{x} + \omega n_t \Delta t)} \quad (1.8)$$

which represents a truncated Fourier series [15] [16] [17]. Unfortunately, due to time constraints in data acquisition, the number of possible sampling points of the \mathbf{k} vector is particularly small, and this leads to Gibbs artefacts [18] [19]. This problem is reflected in *i*) a serious failure of the spectral spatial distribution displacement, and *ii*) a drastic reduction of the image spatial resolution [20] [21].

Several authors have proposed alternative reconstruction methods, in order to *i*) introduce *a priori* physical information into the convolution kernel φ_m and *ii*) exploit mathematical approaches to the MRSI problem no longer affected by the severe aliasing introduced by the necessary spatial frequency truncation [22] [23] [24]. Among others, the SLIM (Spectral Localization by IMaging) method [25] aims to improve the spatial resolution of the spectroscopic image by constraining the solution of the MRSI problem with spatial information. To this end, SLIM models the whole target object by a finite set of compartments whose inner spectroscopic density is supposed to be a constant. The shape and dimensions of these compartments derive from a standard high spatial resolution image of the target.

The BSLIM method [26] further improves the physical description of the MRSI experiment by introducing into the φ_m kernel information regarding the spatially dependent distortions shown by the static magnetic field (B_0).

However, the intrinsic spatial inhomogeneity of the radiofrequency magnetic field (B_1) impacts on the MRSI quantitative potentials as well. It is known that both *i*) the effective depth of penetration and *ii*) the power absorption distribution of the radiofrequency (RF) field show significantly increased spatial inhomogeneity as long as the static magnetic field increases its magnitude [27]. Moreover, in this case the relative B_1 wavelengths should be considered comparable to the size of the human organs to be studied. Thus, B_1 frequency-dependent penetration effects and dielectric resonances result in substantial variations of the actual flip angle throughout the target volume, leading to a spatially variable signal-to-noise-ratio (SNR) as well as to a reduction, spatially modulated, of the contrast [28]. This is reflected in a severe loss of consistency between actual and reconstructed spectral intensities, thus reducing the suitability of MRSI for the clinical query.

Many substantial approaches have been proposed to overcome this problem, most seeking to optimize the experimental conditions either by improving the RF homogeneity over the spectral target [29][30][31], or by reducing the acquisition time [30], or, as a further approach, by developing high sensitivity acquisition techniques [32][33][34]. Although the cited methods have shown their efficacy in improving the experimental conditions, residual B_1 spatial inhomogeneity should nevertheless be considered unavoidable, thus indicating the possible persistence of poor quantitative consistency of the reconstructed data.

An alternative approach could be to use mathematical methods designed to introduce the actual RF spatial distribution into the reconstruction algorithm, thereby adding as much physical information as possible to the $\varphi_m(\mathbf{x}')$ basis functions. To this end, in this paper we propose *starSLIM* (Static and Radiofrequency-compensated SLIM), an evolution of the BSLIM method, in which experimentally derived physical information regarding the B_1 field inhomogeneity map is also included in the transition matrix.

We also present an original method used to acquire this *a priori* information. The proposed method was applied to synthetic raw data and the results obtained are here presented and discussed.

2. Theory.

2.1. Background.

2.1.1. SLIM. The SLIM method assumes that \mathcal{D} , the spectral Field of View (FOV), can be split into L compartments of uniform spectroscopic density. The spatial distribution of each compartment is represented by the functions \mathcal{D}_l ($1 \leq l \leq L$):

$$\mathcal{D}_l(\mathbf{x}) = \begin{cases} 1 & \text{if } \mathbf{x} \in \mathcal{D}_l \\ 0 & \text{otherwise} \end{cases} \quad (2.1)$$

such that

$$\begin{cases} \mathcal{D} = \bigcup_{l=1}^L \mathcal{D}_l(\mathbf{x}) \\ \mathcal{D}_j(\mathbf{x}) \cap \mathcal{D}_h(\mathbf{x}) = \emptyset \quad \text{if } j \neq h \end{cases} \quad (2.2)$$

Thus, the spectral distribution function may be described as

$$\rho_{\text{SLIM}}(\mathbf{x}, \omega) = \sum_{l=1}^L s_l(\omega) \mathcal{D}_l(\mathbf{x}) \quad (2.3)$$

where $s_l(\omega)$ is the unknown spectral function related to the l^{th} compartment. A solution to the spectroscopic problem is then sought computing the coefficients $s_l(\omega)$ such that

$$\{s_l(\omega)\}_{l=1,\dots,L} = \arg \min_{s_l(\omega)} \left\| \mathcal{F}_{(t)}^T [r(\mathbf{k}, t)] - \mathcal{F}_{(\mathbf{x})}^T [\rho_{\text{SLIM}}(\mathbf{x}, \omega)] \right\|^2 \quad (2.4)$$

where $\mathcal{F}_{(dim)}^T[arg]$ is the Discrete Fourier Transform operator applied to the variable $[arg]$ along the dimension (dim) [35] [6].

2.1.2. BSLIM. This model manages the static field inhomogeneity as well as the related magnetic susceptibility effects at the tissue boundaries. This task is achieved by associating a local spectral shift $\Delta\omega(\mathbf{x}) = \gamma\Delta B_0(\mathbf{x})$ with the spatial distribution map $\Delta B_0(\mathbf{x})$ of the static field deviations from the nominal value, thus defining the spectral distribution function as

$$\begin{aligned} \rho_{\text{BSLIM}}(\mathbf{x}, \omega) &= \sum_{l=1}^L s_l(\omega - \Delta\omega(\mathbf{x})) \mathcal{D}_l(\mathbf{x}) \\ &= \sum_{k=1}^K s_l(\omega) e^{-i2\pi\gamma\Delta B_0(\mathbf{x})t} \mathcal{D}_l(\mathbf{x}) \end{aligned} \quad (2.5)$$

In other words, the spatial distribution $\Delta B_0(\mathbf{x})$ behaves as a phase modulation of the unknown spectral distribution. Experimental measurement of $\Delta B_0(\mathbf{x})$ may be performed (after shimming) using, for instance, the AUTOSHIM technique [36]: in this case, the resulting map includes both scanner inhomogeneity as well as magnetic susceptibility effects related to the spectroscopic target.

2.2. Development.

2.2.1. RF spatial inhomogeneity distribution map. An original method for determining the RF inhomogeneity distribution map is here presented.

Acquisition sequences typically used in MRS [37], are based on the combination of a first excitation pulse with several subsequent refocusing pulses involved in the echo formation task.

In MRSI, it is crucial to know the spatial distribution of the flip angle magnitude associated with the excitation pulse: as long as the local flip angle $\alpha(\mathbf{x})$, associated with the deflection of the longitudinal macroscopic magnetization vector $M_z^{(0)}(\mathbf{x})$, differs from the nominal flip angle α_n expected by the acquisition sequence, a systematic error in the spectral density $\rho(\mathbf{x})$ determination, related to the $M_z^{(0)}(\mathbf{x})$ detection, will be introduced into the experiment.

Given a nominal flip angle α_n , we can define the spatial inhomogeneity distribution map associated with the RF magnetic field [38] as

$$\zeta(\mathbf{x}) = \frac{\sin(\alpha(\mathbf{x}))}{\sin(\alpha_n)} \quad (2.6)$$

whose deviations from the unitary ideal value represent the amount of local spectroscopic density that actually contributes to the experimental signal.

Given an acquisition sequence whose excitation pulse is characterized by α_n , the spatial distribution of the signal intensity (i.e. the image of the spectroscopic target) may be expressed as:

$$S(\mathbf{x}; \alpha_n) = \eta(\mathbf{x}) M_z^{(0)}(\mathbf{x}) \sin(\alpha(\mathbf{x})) \quad (2.7)$$

where $M_z^{(0)}(\mathbf{x})$ is associated with the local proton density $\rho(\mathbf{x})$, and $\eta(\mathbf{x})$ is the spatially variable sensitivity response of the receiving coil.

Similarly, acquisition sequences whose excitation pulses are characterized by nominal flip angles $(\frac{\alpha_n}{2})$ and $(\frac{\alpha_n}{2} + \frac{\pi}{2})$ would produce images whose signal intensity distribution map may be expressed as:

$$S\left(\mathbf{x}; \frac{\alpha_n}{2}\right) = \eta(\mathbf{x}) M_z^{(0)}(\mathbf{x}) \sin\left(\frac{\alpha(\mathbf{x})}{2} + \delta(\mathbf{x})\right) \quad (2.8)$$

$$S\left(\mathbf{x}; \frac{\alpha_n}{2} + \frac{\pi}{2}\right) = \eta(\mathbf{x}) M_z^{(0)}(\mathbf{x}) \cos\left(\frac{\alpha(\mathbf{x})}{2} + \varepsilon(\mathbf{x})\right) \quad (2.9)$$

where $\delta(\mathbf{x})$ and $\varepsilon(\mathbf{x})$ are local flip errors, representing possible proportionality breakdown between the nominal flip angle and the flip angle actually experienced by $M_z^{(0)}(\mathbf{x})$.

Since both $\delta(\mathbf{x})$ and $\varepsilon(\mathbf{x})$ are related to the qualitative performances of the RF transmitter, eventual local differences between them, although possible, should not be considered remarkable. In this regard, we here propose the following working hypothesis:

$$\varepsilon(\mathbf{x}) = \delta(\mathbf{x}) + o(\delta(\mathbf{x})) \quad (2.10)$$

Introducing eq.(2.10) into eq.(2.8) and eq.(2.9), and neglecting the $o(\delta(\mathbf{x}))$ term, we can write

$$\begin{aligned}\frac{S(\mathbf{x}; \alpha_n)}{S(\mathbf{x}; \frac{\alpha_n}{2})} &= u(\mathbf{x}) = \frac{\sin(\alpha(\mathbf{x}))}{\sin\left(\frac{\alpha(\mathbf{x})}{2} + \delta(\mathbf{x})\right)} \\ \frac{S(\mathbf{x}; \alpha_n)}{S(\mathbf{x}; \frac{\alpha_n}{2} + \frac{\pi}{2})} &= w(\mathbf{x}) = \frac{\sin(\alpha(\mathbf{x}))}{\cos\left(\frac{\alpha(\mathbf{x})}{2} + \delta(\mathbf{x})\right)}\end{aligned}\quad (2.11)$$

The distributions $u(\mathbf{x})$ and $w(\mathbf{x})$ can both be addressed directly through experimental data acquisitions, as they represent a *pixel-by-pixel* ratio of different images of the spectroscopic target, obtained by implementing the nominal flip angles of interest. Eq.(2.11) is a system of two equations in the unknowns $\alpha(\mathbf{x})$ and $\delta(\mathbf{x})$. We can therefore write

$$\frac{w(\mathbf{x})}{u(\mathbf{x})} = \frac{\sin\left(\frac{\alpha(\mathbf{x})}{2} + \delta(\mathbf{x})\right)}{\cos\left(\frac{\alpha(\mathbf{x})}{2} + \delta(\mathbf{x})\right)} = \tan\left(\frac{\alpha(\mathbf{x})}{2} + \delta(\mathbf{x})\right) \quad (2.12)$$

that is

$$\frac{\alpha(\mathbf{x})}{2} + \delta(\mathbf{x}) = \tan^{-1}\left(\frac{w(\mathbf{x})}{u(\mathbf{x})}\right) \quad (2.13)$$

Introducing eq.(2.13) into the first of eq.(2.11) and considering eq.(2.6), we finally obtain

$$\zeta(\mathbf{x}) = u(\mathbf{x}) \frac{\sin\left(\tan^{-1}\left(\frac{w(\mathbf{x})}{u(\mathbf{x})}\right)\right)}{\sin(\alpha_n)} \quad (2.14)$$

2.2.2. Spectral Distribution Function: B_1 field modelling. Given a spatial inhomogeneity distribution map $\zeta(\mathbf{x})$ of the RF field, the spectral distribution function representing the *starsSLIM* model can be expressed by the relationship

$$\begin{aligned}\rho_{starsSLIM}(\mathbf{x}, \omega) &= \sum_{l=1}^L \zeta(\mathbf{x}) s_l(\omega - \Delta\omega(\mathbf{x})) \mathcal{D}_l(\mathbf{x}) \\ &= \sum_{l=1}^L \zeta(\mathbf{x}) \mathcal{D}_l(\mathbf{x}) s_l(\omega) e^{-i2\pi\gamma\Delta B_0(\mathbf{x})t}\end{aligned}\quad (2.15)$$

where the $\zeta(\mathbf{x})$ map works as an amplitude modulation of the unknown spectral distribution.

In eq.(2.15), effects related to both the major causes of inhomogeneity associated with the magnetic stimulation are carefully distinguished. While inhomogeneity related to the static field is modelled as working on spectral shifting, inhomogeneity in RF power deposition closely relates with the amplitude of the spectral lines. The mathematical description of these experimental instabilities as well as their subsequent introduction into a reconstruction model, should definitively orient the MRSI technique towards quantitative analysis.

2.2.3. *star*SLIM model. Introducing eq.(2.15) into eq.(1.7) we obtain:

$$\begin{aligned} r(\mathbf{k}, t) &= \int_{-\infty}^{\infty} \int_{\mathcal{D}} \rho_{starSLIM}(\mathbf{x}, \omega) e^{-i2\pi(\mathbf{k}\mathbf{x} + \omega t)} d\mathbf{x} d\omega \\ &= \int_{-\infty}^{\infty} \int_{\mathcal{D}} \left(\sum_{l=1}^L \zeta(\mathbf{x}) \mathcal{D}_l(\mathbf{x}) s_l(\omega) e^{-i2\pi\gamma \Delta B_0(\mathbf{x})t} \right) e^{-i2\pi(\mathbf{k}\mathbf{x} + \omega t)} d\mathbf{x} d\omega \end{aligned} \quad (2.16)$$

which can be easily restated as

$$r(\mathbf{k}, t) = \sum_{l=1}^L \int_{-\infty}^{\infty} s_l(\omega) e^{-i2\pi\omega t} d\omega \int_{\mathcal{D}} \zeta(\mathbf{x}) \mathcal{D}_l(\mathbf{x}) e^{-i2\pi\gamma \Delta B_0(\mathbf{x})t} e^{-i2\pi\mathbf{k}\mathbf{x}} d\mathbf{x} \quad (2.17)$$

The integral

$$u_l(t) = \int_{-\infty}^{\infty} s_l(\omega) e^{-i2\pi\omega t} d\omega \quad (2.18)$$

can be identified as the signal, as a function of time, related to the l^{th} compartment; eq.(2.17) may thus be rewritten as

$$r(\mathbf{k}, t) = \sum_{l=1}^L u_l(t) \int_{\mathcal{D}} \zeta(\mathbf{x}) \mathcal{D}_l(\mathbf{x}) e^{-i2\pi\gamma \Delta B_0(\mathbf{x})t} e^{-i2\pi\mathbf{k}\mathbf{x}} d\mathbf{x} \quad (2.19)$$

In this paper, we propose a definition of a spectral amplitude modulation function such that

$$\xi_l(\mathbf{x}) = \zeta(\mathbf{x}) \mathcal{D}_l(\mathbf{x}) = \begin{cases} \zeta(\mathbf{x}), & \text{if } \mathbf{x} \in \mathcal{D}_l \\ 0, & \text{otherwise} \end{cases} \quad (2.20)$$

The spatial distribution of $\xi_l(\mathbf{x})$ represents the RF inhomogeneity distribution related to the l^{th} compartment. On this basis, eq.(2.19) may be restated as

$$r(\mathbf{k}, t) = \sum_{l=1}^L u_l(t) \int_{\mathcal{D}} \xi_l(\mathbf{x}) e^{-i2\pi\gamma \Delta B_0(\mathbf{x})t} e^{-i2\pi\mathbf{k}\mathbf{x}} d\mathbf{x} \quad (2.21)$$

The integral kernel of the spectral operator may then be defined as

$$\begin{aligned} \mathcal{H}_l(\mathbf{k}, t) &= \int_{\mathcal{D}} \xi_l(\mathbf{x}) e^{-i2\pi\gamma \Delta B_0(\mathbf{x})t} e^{-i2\pi\mathbf{k}\mathbf{x}} d\mathbf{x} \\ &= \int_{\mathcal{D}} \xi_l(\mathbf{x}) e^{-i2\pi\Delta\omega(\mathbf{x})t} e^{-i2\pi\mathbf{k}\mathbf{x}} d\mathbf{x} \end{aligned} \quad (2.22)$$

The experimental measure of a spectroscopic signal could be rewritten in the form of a linear system of equations

$$r(\mathbf{k}, t) = \sum_{l=1}^L u_l(t) \mathcal{H}_l(\mathbf{k}, t) \quad (2.23)$$

Thus, the above equation may be restated as a minimization problem: given N sampling points along the temporal dimension and given M sampling points along the phase-encoding dimension of the spectroscopic K-space, for each experimental datum $r(\mathbf{k}_m, n\Delta t)$ ($m = 1, 2, \dots, M$ and $n = 1, 2, \dots, N$) the L values of the unknown spectroscopic FID, as evaluated at the n^{th} sampling point, can be obtained as

$$\{u_l(n\Delta t)\}_{l=1,\dots,L} = \arg \min_{u_l(n\Delta t)} \sum_{m=1}^M \left\| r(\mathbf{k}_m, n\Delta t) - \sum_{l=1}^L u_l(n\Delta t) \mathcal{H}_l(\mathbf{k}_m, n\Delta t) \right\|^2 \quad (2.24)$$

2.2.4. Computational algorithm. For each temporal sampling point $n\Delta t$, eq.(2.23) represents a system of linear equations that can be rewritten in matrix form, such that

$$\mathcal{H}\mathbf{u} = \mathbf{r} \quad (2.25)$$

where

- \mathcal{H} is the $(M \times L)$ system matrix, with rank P ,
- \mathbf{u} is the $(L \times 1)$ vector of unknowns,
- \mathbf{r} is the $(M \times 1)$ vector of experimental data

associated with the n^{th} sampling point.

Using a standard singular value decomposition for the \mathcal{H} system matrix

$$\mathcal{H} = \mathbf{U}\mathbf{\Sigma}\mathbf{V}^* \quad (2.26)$$

where \mathbf{U} and \mathbf{V} are isometric matrices, $\mathbf{\Sigma}$ is a diagonal matrix whose elements σ_p are the singular values of \mathcal{H} and \mathbf{V}^* is the adjoint of \mathbf{V} , then a solution for eq.(2.25) is sought such that

$$\widetilde{\mathbf{u}}_p = \frac{\widetilde{\mathbf{r}}_p}{\sigma_p} \quad (2.27)$$

where $\widetilde{\mathbf{u}}_p = \mathbf{V}^* \mathbf{u}$, $\widetilde{\mathbf{r}}_p = \mathbf{U}^* \mathbf{r}$ and $p = 1, 2, \dots, P$.

With respect to the incorporation of $\zeta(\mathbf{x})$ into the system matrix, it could be worth noting that the integral kernel in eq.(2.22) may be framed as

$$\mathcal{H}_l(\mathbf{k}, t) = \mathcal{F}_{(\mathbf{x})}^T [\mathcal{F}_t^T [\zeta(\mathbf{x}) \mathcal{D}_l(\mathbf{x}) \delta(\omega - \Delta\omega(\mathbf{x}))]] \quad (2.28)$$

In other words, an image of the integral operator \mathcal{H}_l in a four-dimensional space (\mathbf{x}, ω) exists: such an image can be written as

$$\psi_l(\mathbf{x}, \omega) = \zeta(\mathbf{x}) \mathcal{D}_l(\mathbf{x}) \delta(\omega - \Delta\omega(\mathbf{x})) \quad (2.29)$$

representing a Dirac delta-like impulse δ , associated with the spatial coordinate $\mathbf{x} \in \mathcal{D}_l$ and located at the spectral shift $\Delta\omega(\mathbf{x})$ in the frequency domain, whose amplitude is modulated by the RF inhomogeneity value $\zeta(\mathbf{x})$. *A priori* physical information regarding *i)* the spatial distribution of the spectral target, *ii)* the B_0 distribution map and *iii)* the RF distribution map, are then introduced into the minimization problem (eq.(2.24)) as described by eq.(2.28).

3. Raw Data Simulation. To test the behaviour of the proposed algorithm, synthetic raw data reproducing a standard 3D-CSI spectroscopic k-space were generated. The simulation software, as well as the reconstruction software reproducing the

starslim method, were written in MATLAB[®] (MathWorks, 3 Apple Hill Drive, Natick, Massachusetts, USA).

Forty-five spectroscopic compartments were extracted from a *in vivo* high resolution mediotthalamic T_2 -weighted anatomical image of a normal human brain, as illustrated in Fig.(3.1). Specific software for the segmentation step was designed and created. The aim, in choosing to simulate a large number of compartments, was to succeed

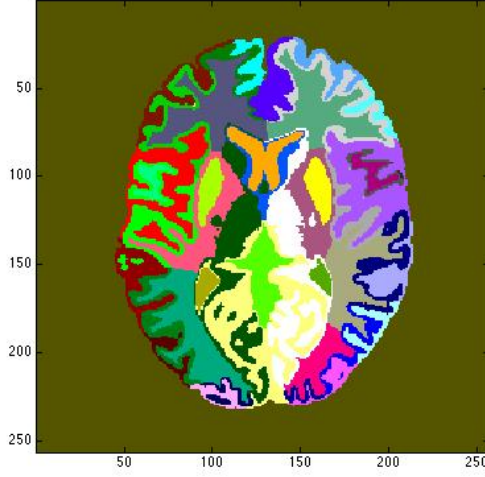


Figure 3.1: Compartment image. Forty-five anatomically shaped compartments were extracted by means of a segmentation process. Each compartment is represented by a different color.

in characterizing the behaviour of the model when *i)* both the area and the shape of the compartment are subjected to severe variations and, more significantly, when *ii)* the compartments imbricate with each other, since this is a situation typically encountered in *in vivo* studies.

The segmentation software was designed to identify compartments whose shape reflects anatomical boundaries between neighbouring tissues. In this work, when compartments having an extensive area were extracted, they were arbitrarily split into two or three smaller compartments, thereby increasing the spatial complexity of the spectroscopic target and, as a consequence, also increasing the number of unknowns in the reconstruction process. This increase exacerbates the numerical instability of the inverse problem under evaluation, thus subjecting to stress the restoration ability of the proposed method.

For each compartment, a composite spectrum was simulated. Each spectrum was composed of two or three spectral peaks of unitary amplitude. The characteristic frequency of each peak was randomly generated in the range $[-400, 0]$ Hz; T_2 damping factors associated with each peak were also randomly generated, in the range $[50, 1200]$ ms. On this basis, we generated a noise-free and a noisy k-space, the latter characterized by a SNR of 15.7 dB. For both of them, the spectroscopic dimension was sampled in 1024 points, corresponding to a 2kHz bandwidth. The chosen number of phase encoding steps was equal to 8×8 .

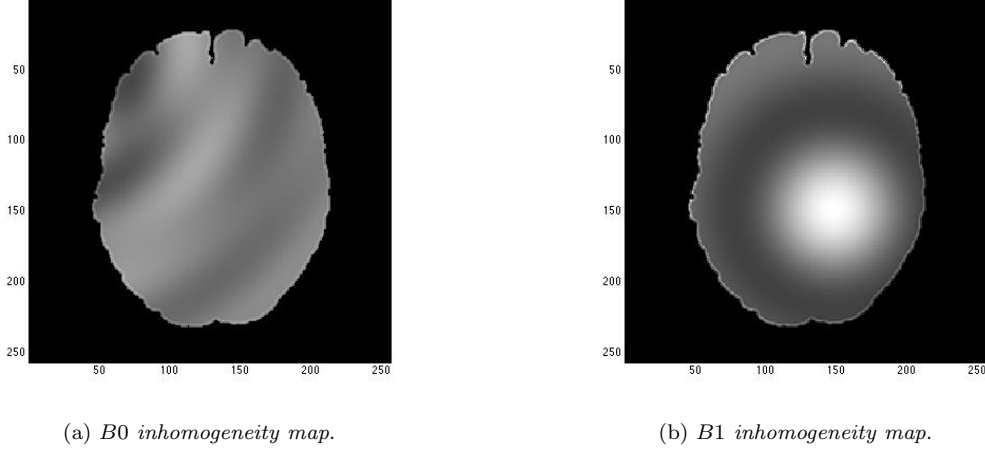


Figure 3.2: Images representing the inhomogeneity distribution maps

The static magnetic field inhomogeneity map employed in the simulation task is represented in Fig.(3.2). To simulate the effects of changes in magnetic susceptibility at the tissue-air interface, the original image was filtered using a Laplacian of a Gaussian filter ($FWHM = 2$, in pixel units). The smooth 2D variation in map intensity was calculated to simulate a static field variation corresponding to a maximum of 2 *ppm* in frequency equivalent units.

The same approach was followed for simulation of the RF magnetic field inhomogeneity map. A 2D *sinc* function spanning the non null part of the target image was reproduced; its amplitude was modulated such that the relative $\zeta(\mathbf{x})$ map (eq.(2.14)) falls in the range of $[0.3, 1]$.

4. Results. The method presented in this paper was tested comparing results from reconstructions of synthetic k-spaces with those obtained from reconstructions of the same raw data sets performed using both SLIM and BSLIM methods.

To avoid possible computational discrepancies deriving from the software used for each of the tested methods, the SLIM and BSLIM algorithms were reproduced running the same computational code used for the *starslim* model. In detail, SLIM was implemented by *i*) setting to zero the uniformity map amplitude, related to the static magnetic field, and *ii*) transforming the RF inhomogeneity map into a uniform unitary distribution, while the latter point alone was used to reproduce the BSLIM method. To simulate the static magnetic field distribution, the inhomogeneity distribution map described in the previous paragraph was implemented.

Reconstructed spectra from noiseless and 15.7 dB SNR raw data sets are shown. Results from different compartments are shown in order to highlight the behaviour of the reconstruction model in the presence of various compartment morphologies. Each reconstructed spectrum is graphically superimposed on the corresponding true spectrum.

4.1. noiseless raw data. Spectra from reconstructions of noiseless k-space are shown in Fig.(4.1): they constitute a valuable starting point for a robust description of the results obtained. Spectra from the *starslim* method reproduce the true data sets with outstanding consistency, determining both their characteristic frequencies and their amplitudes. This result is independent of the size of the compartment under evaluation. It is particularly interesting to consider the analysis of the results given by both the SLIM and BSLIM methods. The latter, while apparently able to correctly address the characteristic frequencies of the simulated peaks, fails to reproduce their amplitudes; on the other hand, the SLIM method fails to fix either amplitudes or characteristic frequencies. Moreover, spurious peaks can be observed with both these reconstruction methods. When compartments with a smaller total area were considered (compartment 9, for instance), the magnitude of spurious peaks was found to be increased.

In this respect, a thorough analysis of the spectral spillover between neighbouring compartments was conducted. Fig.(4.2) shows evidence of possible spillover into a small compartment induced by a larger adjacent compartment. With the *starslim* model, no evidence of spillover peaks can be found. On the contrary, the SLIM and BSLIM methods both appear strongly affected by spectral spillover effect, as the plots in Fig.(4.2c) and Fig(4.2d) clearly demonstrate.

To investigate the possible dependence of the spillover effect on the relative magnitude of the compartments under evaluation, equivalent analyses were performed between both *i)* compartments of comparable magnitude and *ii)* compartments of clearly different magnitude. The results from the first of these analyses are reported in Fig.(4.3), where the cross-talk effect appears minimal if not absent. Results from the second analysis are reported in Fig.(4.4). Here, the presence of intra-compartment cross-talk confirmed the results illustrated in Fig.(4.2c) although, in this case, the compartments under analysis were neither contiguous nor imbricated with each other.

4.2. noisy raw-data. The synthetic raw data set characterized by 15.7 dB SNR was also processed. Once reconstructed, no noise reduction procedures were applied to the spectral results, presented in Fig.(4.5). To support a straightforward comparison of the reconstruction models of interest, the reported spectra refer to the same compartments presented in Fig.(4.1). The remarks on the results obtained from the noiseless raw data set seem to apply the present case too. The only minor difference concerns the *starslim* method, as the low SNR prevents the reconstructed spectra from properly fitting the simulated peak amplitudes.

On the other hand, as regards inter-compartment spectral spillover, Figs (4.6), (4.7) and (4.8) propose a comparative analysis following the same scheme already presented for the noise-free raw data. The dependence of spectral spillover on both the relative compartment size and the relative compartment position, as inferred from the noise-free data analysis, is confirmed.

5. Discussion. In this paper, a 3D modelling approach for the reconstruction of high spatial resolution MRS images has been presented. With this approach, as with the original SLIM method, a solution is sought by performing an eigen-decomposition of the transition matrix, defined on L^2 Hilbert spaces, thus identifying the null space of the transformation operator and, simultaneously, obtaining a least squares solution. As reported in this paper, the ill-posedness of the transition matrix was reduced (with respect to the SLIM method) by introducing *a priori* physical information concerning the signal detection process. Essentially, this paper deals with *i)* a spatially dependent frequency modulation, related to the inhomogeneity distribution map of

the static magnetic field and already addressed by other reconstruction models [14] [26], and *ii*) a spatially dependent modulation amplitude map (the objective of the present method) derived from the inhomogeneity distribution map of the RF field. With regard to this latter point, an original approach for the experimental detection of this basic information has herein been presented too.

The intrinsic spatial distribution of a given metabolite into a biological tissue is obviously considered a spatially variant physiological parameter. However, the original SLIM method starts from the assumption that the spatial distribution of the compartmental spectral density is a constant, leaving the task of overcoming the latter limiting hypothesis to a generalized series extension (GSLIM: Generalized SLIM) of the spectral density model [39]:

$$\rho_{\text{GSLIM}}(\mathbf{x}, \omega) = \sum_{m=1}^M a_m(\omega) \varphi_m(\mathbf{x}, \omega) \quad (5.1)$$

where $a_m(\omega)$ coefficients represent the unknown spectra and $\varphi_m(\mathbf{x}, \omega)$ are basis functions, as already introduced by eq.(1.4).

In GSLIM, the choice for the basis functions was such that

$$\varphi_m(\mathbf{x}, \omega) = \rho_{\text{SLIM}}(\mathbf{x}, \omega) e^{i2\pi \mathbf{k}_m \mathbf{x}} \quad (5.2)$$

thus leading to the following spectral function

$$\rho_{\text{GSLIM}}(\mathbf{x}, \omega) = \rho_{\text{SLIM}}(\mathbf{x}, \omega) \sum_{m=1}^M a_m(\omega) e^{i2\pi \mathbf{k}_m \mathbf{x}} \quad (5.3)$$

This equation deserves in-depth comment. Taking the $\rho_{\text{SLIM}}(\mathbf{x}, \omega)$ basis as our starting point, the intra-compartment homogeneity constraint is supposed to be broken through the $e^{i2\pi \mathbf{k}_m \mathbf{x}}$ oscillating term, leaving it up to the unknown amplitude modulation coefficients $a_m(\omega)$ to solve the incongruities between the raw data set and the proposed mathematical modelization of the spectroscopic experiment.

Actually, this task is unlikely to be fulfilled. The ρ_{SLIM} spectral distribution derives from the solution of a linear system whose transition operator [25] does not account for the spatial distribution of either the RF field, or the static magnetic field. As a consequence of this latter issue, the reconstructed frequency peaks are expected to represent a systematic frequency shift with respect to the true frequency distribution reproduced by the synthetic data set. This datum is confirmed by the previously reported analysis of the results. Thus, the $a_m(\omega)$ coefficients should be considered to be prevented from fitting the true spectral peaks, given that the reconstructed characteristic frequencies to which they refer are not actually represented in the true raw data set.

On the other hand, eq.(5.3) could also be restated by replacing ρ_{SLIM} with the ρ_{BSLIM} density function, the latter representing a reconstruction model (eq.(2.5)) whose computational kernel does actually include the static field inhomogeneity map, even though it disregards the actual amount of magnetic energy transferred to the detection devices as a consequence of the RF stimulation. Thus, the reconstructed frequency peaks, although addressing the true frequency distribution, fail to reproduce their amplitudes, as shown in the previous paragraph. In this case, $a_m(\omega)$ coefficients should simultaneously modulate for both *i*) the physiological spatial variation of metabolite intensity and *ii*) the amplitude of the RF field deposition. Of course, this approach

could only lead to a compromise solution, whose apparent meaning, when the absolute quantification of the spectral components is under evaluation, will clearly be misleading.

The above discussion should highlight the importance of including in the reconstruction process physical information concerning the B_1 magnetic field. In this case, eq.(5.3) may be written as

$$\rho_{\text{GSLIM}}(\mathbf{x}, \omega) = \rho_{\text{starSLIM}}(\mathbf{x}, \omega) \sum_{m=1}^M a_m(\omega) e^{i2\pi \mathbf{k}_m \mathbf{x}} \quad (5.4)$$

where the a_m coefficients are linked only to amplitude modulations fitting the physiology of the metabolite distribution, the physical inhomogeneities of the experimental set-up being entirely charged into the ρ_{starSLIM} distribution.

The simulation of experimental spectroscopic raw data sets should be considered a sensitive tool in reconstruction model evaluation tasks. In this paper, lack of model consistency with respect to the simulated experimental conditions has been shown to translate into both *i)* a mathematical corruption of the solution, leading to the appearance of randomly distributed spurious peaks and *ii)* spectral cross-talk (spillover) between compartments.

With respect to this latter issue, the spectra reported in Fig.(4.4) show that the spillover effect should be considered a severe cause of solution blurring even between non-contiguous compartments. This result is independent (Fig.(4.8)) of the presence of noise in the raw data set. The spectra in Fig.(4.2) and Fig.(4.3) demonstrate that the amount of spillover is related to the relative inter-compartment signal magnitude: when compartments of comparable size are considered, the spillover effect, if it has not completely vanished, is negligible. Moreover, the plots reported in Fig.(4.6) and Fig.(4.7) suggest that the influence of spectral noise in spillover artefacts should be considered limited [40] [41].

Although simulated spectroscopic data are an extremely valuable numerical basis for the assessment of a mathematical model, experimental data from a physical phantom might add consistency to the proposed method. Nevertheless, physical phantoms where two or three compartments at most are reproduced should be considered of minor significance. In fact, in the case of discrete sampling, using the formalism introduced in eq.(1.1) a generic inverse problem may be stated in the form [1]

$$\mathbf{A}f^{(0)} = \sum_{k=1}^p \sigma_k(f^{(0)}, v_k)_{\mathcal{X}} u_k \quad (5.5)$$

where σ_k are the singular values of \mathbf{A} , p is the rank of \mathbf{A} and v_k and u_k are the singular vectors of \mathcal{X} and \mathcal{Y} , respectively. The severity of the ill-conditioning is given by the condition number

$$\alpha = \frac{\sigma_1}{\sigma_p} \quad (5.6)$$

Thus, transforming a continuous variable into a finite number of samples influences the ill-conditioning of the problem, lowering, as a primary consequence, the relative condition number as the number of samples decreases. In this paper, the decision to test the *starSLIM* model using a high number of compartments was based on these considerations. A physical phantom suitable for the assessment of MRSI reconstruction algorithms, should thus be composed of certain selected biological metabolites

embedded into a number (e.g. 12-15) of cellular (or specific gel) bases sealed in small vials. The latter could then be organized into a rigid, regularly spaced lattice, thus forming the core of a valid and meaningful physical phantom.

The method for obtaining experimental derivation of the B_1 field inhomogeneity map presented in this paper offers several further points for discussion.

The power deposition distribution map may be influenced by the magnitude of the flip angle associated with the excitation pulse. In this respect, the proposed method easily reproduces the actual spectroscopic excitation. In fact, the α_n flip angle in eq.(2.7) is not submitted to numerical constraints, with the exclusion, of course, of the case $\alpha_n = \pi$: a flip value that, not representing an actual magnetic energy excitation, should not be considered of interest.

A second point is related to the observation that eq.s (2.7), (2.8) and (2.9) consider the whole longitudinal magnetization vector $M_z^{(0)}(\mathbf{x})$ as contributing to the signal intensity distribution. This implies that the sequence repetition time TR is much longer than the $T1$ time constant representing the relaxation parameter for the longitudinal magnetization, thus leading to relatively long imaging times that might give rise to motion artefact issues. Nevertheless, in the case of an acquisition sequence whose stimulation pulses reproduce the $\{\alpha_n, \frac{\alpha_n}{2}, \frac{\alpha_n}{2} + \frac{\pi}{2}\}$ series, the longitudinal magnetization recovery after the first excitation pulse (α_n flip angle) may be easily described by

$$M_z^{(\alpha_n)}(\mathbf{x}, t) = M_z^{(0)}(\mathbf{x}) \cos(\alpha_n) e^{-\frac{t}{T1}} + M_z^{(0)}(\mathbf{x}) (1 - e^{-\frac{t}{T1}}) \quad (5.7)$$

If $TR_{\frac{\alpha_n}{2}}$ is the time interval occurring between the first (α_n flip) and the second ($\frac{\alpha_n}{2}$ flip) pulses, then eq.(2.8) may be rewritten as

$$S\left(\mathbf{x}; \frac{\alpha_n}{2}\right) = \eta(\mathbf{x}) M_z^{(\alpha_n)}(\mathbf{x}, TR_{\frac{\alpha_n}{2}}) \sin\left(\frac{\alpha(\mathbf{x})}{2} + \delta(\mathbf{x})\right) \quad (5.8)$$

Similarly, the longitudinal magnetization recovery after the second excitation pulse ($\frac{\alpha_n}{2}$ flip angle) may be written as

$$M_z^{(\frac{\alpha_n}{2})}(\mathbf{x}, t) = M_z^{(\alpha_n)}(\mathbf{x}, TR_{\frac{\alpha_n}{2}}) \cos\left(\frac{\alpha_n}{2}\right) e^{-\frac{t}{T1}} + M_z^{(0)}(\mathbf{x}) (1 - e^{-\frac{t}{T1}}) \quad (5.9)$$

leading to the image intensity distribution

$$S\left(\mathbf{x}; \frac{\alpha_n}{2} + \frac{\pi}{2}\right) = \eta(\mathbf{x}) M_z^{(\frac{\alpha_n}{2})}(\mathbf{x}, TR_{\frac{\alpha_n}{2} + \frac{\pi}{2}}) \cos\left(\frac{\alpha(\mathbf{x})}{2} + \varepsilon(\mathbf{x})\right) \quad (5.10)$$

where $TR_{\frac{\alpha_n}{2} + \frac{\pi}{2}}$ is the time interval occurring between the second ($\frac{\alpha_n}{2}$ flip) and the third ($\frac{\alpha_n}{2} + \frac{\pi}{2}$ flip) stimulation pulses. If the experimental requirements demand an acquisition sequence whose $TR \approx T1$, eq.s (2.8) and (2.9) may be usefully replaced by eq.s (5.8) and (5.10) respectively, thus making it possible to correct the spectroscopic target images for the signal intensity leakage due to incomplete longitudinal magnetization recovery.

6. Conclusions. The reliability of the MRSI technique as an investigation tool depends on two main factors: *i)* accurate spatial localization and *ii)* quantitative consistency of the reconstructed spectra. With respect to the latter factor, obstacles may arise because spatially distributed B_0 and B_1 magnetic field inhomogeneities may affect the spectroscopic significance of the raw data set.

Based on the approach adopted by SLIM, the method described in this paper is proposed as a possible new solution for 3D inverse problem in MRSI. As demonstrated by the synthetic experiments reported, the introduction of the B_1 field inhomogeneity map into the reconstruction kernel determines *i)* the possibility of reproducing the intensities of the actual metabolite peaks, thus improving the quantitative reliability characteristic of MRSI and *ii)* the possibility of reducing the condition number of the associated inverse problem, thus reducing the influence of raw-data noise on the numerical stability of the reconstructed spectra.

These characteristics may lead to consideration of the *starSLIM* method for *in vivo* applications.

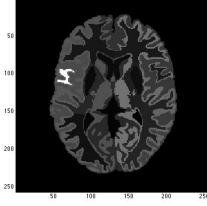
Acknowledgments. The authors wish to thank Dr Catherine Wrenn for her valuable assistance in preparing the manuscript.

This work was supported by the Interdepartmental Centre of Research on Magnetic Resonance (CIRM) as well as by the Interdepartmental Centre for the Pre-Clinical Development of Molecular Imaging (CISPIM) of the University of Florence.

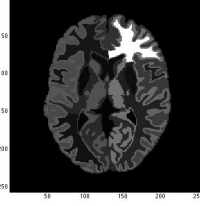
REFERENCES

- [1] Bertero M and Boccacci P. *Introduction to inverse problems in imaging*. Institute of Physics Publisher, Bristol and Philadelphia, 1998.
- [2] Morozov VA. Regularization methods for ill-posed problems. *CRC Press*, 1993.
- [3] Tikhonov AN and Arsenin VY. *Solutions of Ill-Posed Problems*. Winston and sons, Washington DC, 1977.
- [4] Bierens J. *Hilbert space theory and its applications to semi-nonparametric modeling and inference*. Pennsylvania State University, 2012.
- [5] Pouillet JB, Sima DM and Van Huffel S. MRS signal quantification: A review of time and frequency-domain methods. *J Magn Reson*, 195(2):134–144, 2008.
- [6] Golub GH and Van Loan CF. *Matrix Computations*. The Johns Hopkins University Press, 1983.
- [7] Aster RC, Borchers B and Thurber CH. *Parameter Estimation and Inverse Problems*. Elsevier Academic Press, USA, 2005.
- [8] Tarantola A. Inverse problem theory and methods for model parameter estimation. *SIAM*, 2005.
- [9] Barker PB, Bizzi A, De Stefano N, Gullapalli RP and Lin DDT. *Clinical MR Spectroscopy. Techniques and Applications*. Cambridge University Press, UK, 2010.
- [10] de Graff RA. *In vivo NMR spectroscopy: principles and techniques*. Wiley, New York, 1998.
- [11] Chrysikopoulos HS. Chemical shift imaging. In *Clinical MR Imaging and Physics*, pages 52–55. 2009.
- [12] Mitchell DG and Cohen MS. Chemical shift. In *MRI Principles*, chapter 5, pages 49–56. 2004.
- [13] Brown TR, Kincaid BM and Ugurbil K. NMR chemical shift imaging in three dimensions. *Proc Natl Acad Sci USA*, 79(11):3523–3526, 1982.
- [14] Bashir A and Yablonskiy D. Natural linewidth chemical shift imaging (NL-CSI). *Magn Reson Med*, 56(1):7–18, 2006.
- [15] Bracewell RN. *The Fourier Transform and its applications*. McGraw-Hill, 1986.
- [16] Bracewell RN. *Fourier Analysis and Imaging*. Plenum, 2004.
- [17] Sarkar S, Heberlein K and Hu XP. Truncation artifact reduction in spectroscopic imaging using a dual-density spiral k-space trajectory. *Magn Reson Imaging*, 20(10):743–757, 2002.
- [18] Gao Y and Reeves SJ. Optimal k-space sampling in MRSI for images with a limited region of support. *IEEE Trans Med Imag*, 19(12):1168–1178, 2000.
- [19] Oppenheim AV and Schaffer RW. *Discrete-Time Signal Processing*. Prentice Hall, 1989.
- [20] Liang ZP. *Constrained Image Reconstruction from Incomplete and Noisy Data: A New Parametric Approach*, 1989.
- [21] Liang ZP and Haacke EM. Parametric imaging: overcoming the gibbs artifact. *Magn Reson Imaging*, 8(1):253, 1990.
- [22] Haacke EM, Liang ZP and Izen SH. Contrained reconstruction: a superresolution, optimal signal-to-noise alternative to the fourier transform in magnetic resonance imaging. *Med Phys*, 16(3):388–397, 1989.
- [23] Liang ZP and Lauterbur PC. Constrained imaging: overcoming the limitations of the fourier series. *IEEE EMB Magazine*, 15:126–132, 1996.
- [24] Wear KA, Myers KJ, Rajan SS and Grossman LW. Constrained reconstruction applied to 2-D chemical shift imaging. *IEEE Trans Med Imag*, 16(5):591–597, 1997.
- [25] Hu X, Levin DN, Lauterbur PC and Spraggins T. SLIM: Spectral Localization by Imaging. *Magn Reson Med*, 8:314–322, 1988.
- [26] Khalidov I, Van De Ville D, Jacob M, Lazeyras F and Unser M. BSLIM: spectral localization by imaging with explicit B0 field inhomogeneity compensation. *IEEE Trans Med Imaging*, 26(7):990–1000, 2007.
- [27] Roschmann P. Radiofrequency penetration and absorption in the human body: Limitations to high-field whole-body nuclear magnetic resonance imaging. *Med Phys*, 14(6):922–931, 1987.
- [28] Hoult DI, Phil D. Sensitivity and power deposition in a high-field imaging experiment. *J Magn Reson Imaging*, 12:46–67, 2000.
- [29] Hetherington HP, Avdievich NI, Kuznetsov AM, and Pan JW. RF shimming for spectroscopic localization in the human brain at 7 T. *Magn Reson Med*, 63:9–19, 2010.
- [30] Geppert C, Dreher W, Althaus M, and Leibfritz D. Fast ^1H spectroscopic imaging using steady state free precession and spectral-spatial RF pulses. *MAGMA*, 19(4):196–201, 2006.
- [31] Hoult DI and Deslauriers R. A high-sensitivity, high- b_1 homogeneity probe for quantitation of metabolites. *Magn Reson Med*, 16(3):411–417, 1990.
- [32] Henning A, Schar M, Schulte RF, Wilm B, Pruessmann KP, and Boesiger P. SELOVS: brain

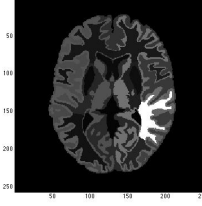
- MRSI localization based on highly selective T_1 - and B_1 - insensitive outer volume suppression at 3T. *Magn Reson Med*, 59(1):40–51, 2008.
- [33] Snyder J and Wilman A. Field strength dependence of PRESS timings for simultaneous detection of glutamate and glutamine from 1.5 to 7 T. *J Magn Reson*, 203(1):66–72, 2010.
 - [34] Schirda CV, Tanase C, and Boada FE. Rosette spectroscopic imaging: optimal parameters for alias free, high sensitivity spectroscopic imaging. *J Magn Reson Imaging*, 29(6):1375–1385, 2009.
 - [35] Landi G and Loli Piccolomini E. Fast methods for MR spectroscopic imaging. *Applied Mathematics and Computation*, 191:389–396, 2007.
 - [36] Schneider E and Glover G. Rapid in vivo proton shimming. *Magn Reson Med*, 18(2):335–347, 1991.
 - [37] Bernstein MA, King KF and Zhu XJ. *Handbook of MRI Pulse Sequences*. Elsevier Academic Press, 2004.
 - [38] Truong TK, Chakeres DW, Beversdorf DQ, Scharre DW and Schmalbrock P. Effects of static and radiofrequency magnetic field inhomogeneity in ultra-high field magnetic resonance imaging. *Magn Reson Imaging*, 24(2):103–112, 2006.
 - [39] Liang ZP and Lauterbur PC. A generalized series approach to mr spectroscopic imaging. *IEEE Trans Med Imaging*, 10(2):132–137, 1991.
 - [40] Lang S. *Complex Analysis*. Springer, 1998.
 - [41] Pijnappel WWF, van den Boogart A, de Beer R and van Ormondt D. SVD-based quantification of magnetic resonance signals. *J Magn Res*, 97(1):122–134, 1992.



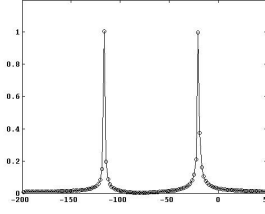
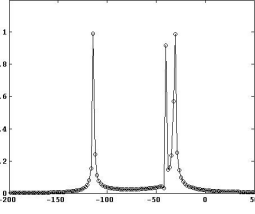
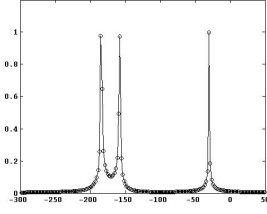
(a) *Compartment 9.*



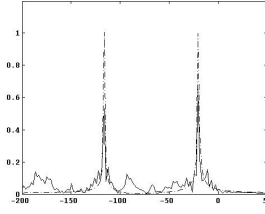
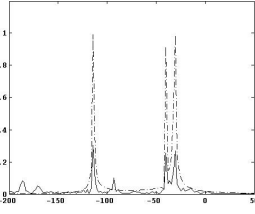
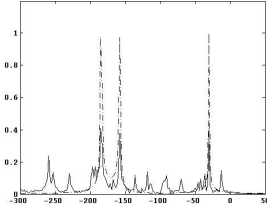
(b) *Compartment 11.*



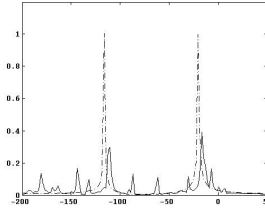
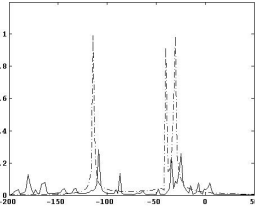
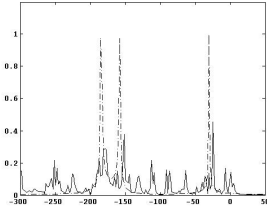
(c) *Compartment 14.*



(d) *starSLIM method. Simulated (i.e. true) spectra are represented by circles.*

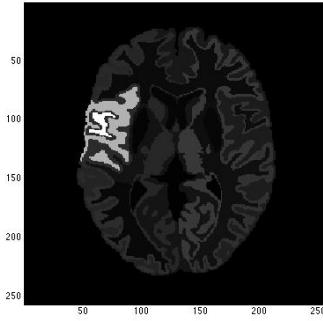


(e) *BSLIM method. Simulated (i.e. true) spectra are represented by dash and dot line style.*

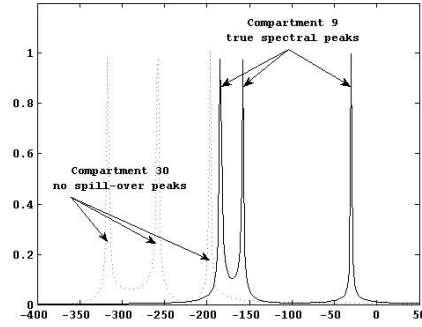


(f) *SLIM method. Simulated (i.e. true) spectra are represented by dash and dot line style.*

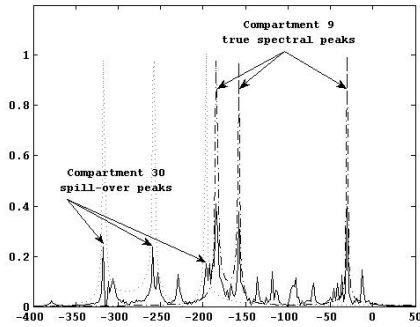
Figure 4.1: Spectra resulting from the reconstruction of the noiseless data set, relating to compartments 9, 11 and 14. For each compartment, reconstructed (continuous lines) and simulated spectra are in a manner designed to facilitate the comparison. Spectra from different reconstruction methods are ordered by columns. With the *starSLIM* method there is correct matching of both amplitude and frequency characteristic values.



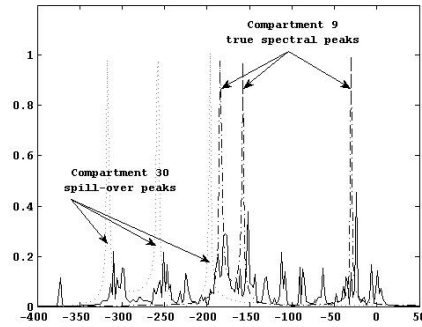
(a) Compartment 9 (white) and Compartment 30 (light gray).



(b) starslim method.

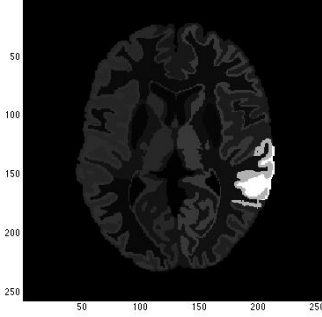


(c) BSLIM method.

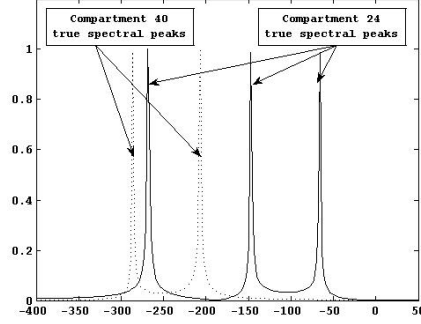


(d) SLIM method.

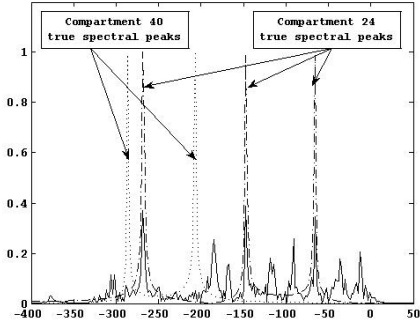
Figure 4.2: Reconstructed spectra (continuous lines) from the noiseless raw data set, relating to compartment 9. Plot 4.2b refers to the starslim method: there is no evidence of spillover peaks from compartment 30. On the contrary, plots for the BSLIM and the SLIM method show strong spillover components.



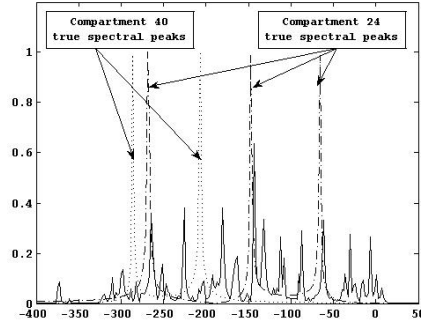
(a) Compartment 24 (white) and Compartment 40 (light gray).



(b) starsSLIM method.

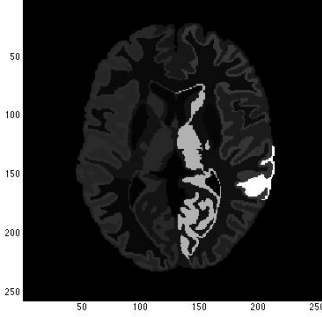


(c) BSLIM method.

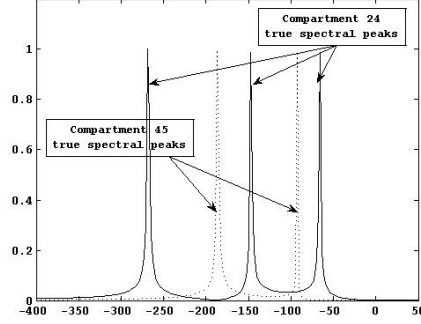


(d) SLIM method.

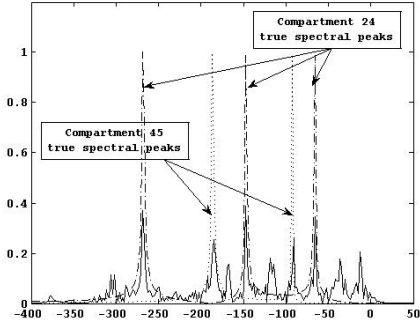
Figure 4.3: Reconstructed spectra (continuous lines) from the noiseless raw data set, relating to compartment 24. Plot 4.3b refers to the starsSLIM method: there is no evidence of spillover peaks from compartment 40. In this case, because of the limited size of compartment 40, spectra from both the BSLIM and the SLIM method also fail to show evidence of frequency peaks deriving from the spillover effect.



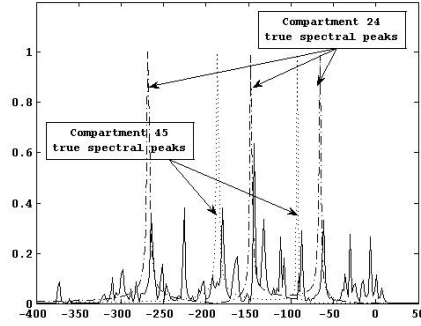
(a) Compartment 24 (white) and Compartment 45 (light gray).



(b) starsSLIM method.

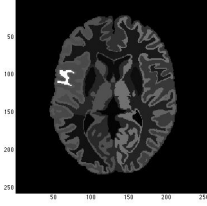


(c) BSLIM method.

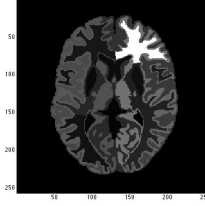


(d) SLIM method.

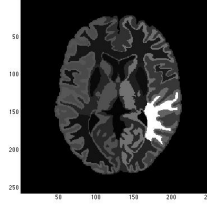
Figure 4.4: Reconstructed spectra (continuous lines) from the noiseless raw data set, relating to compartment 24. Plot 4.4b refers to starsSLIM method: in this case too, there is no evidence of spillover peaks from compartment 45. On the other hand, because of the large size of compartment 45 and despite its spatial shifting, spectra from the both BSLIM and SLIM method show evidence of frequency peaks spilling over from compartment 45.



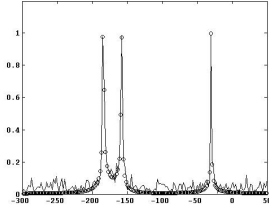
(a) *Compartment 9.*



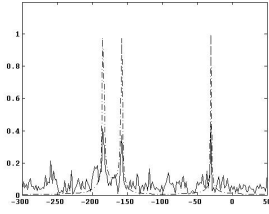
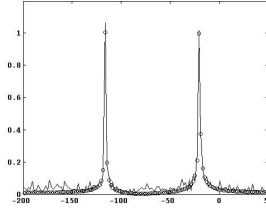
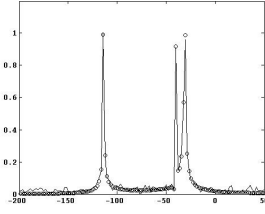
(b) *Compartment 11.*



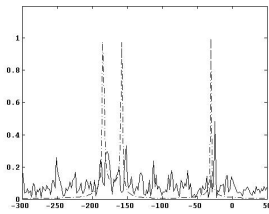
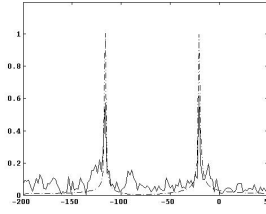
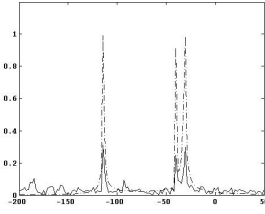
(c) *Compartment 14.*



(d) *starsSLIM method. Simulated (i.e. true) spectra are represented by circles.*



(e) *BSLIM method. Simulated (i.e. true) spectra are represented by dash and dot line style.*



(f) *SLIM method. Simulated (i.e. true) spectra are represented by dash and dot line style.*

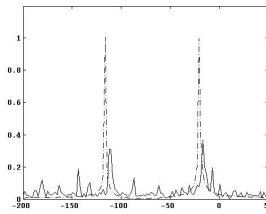
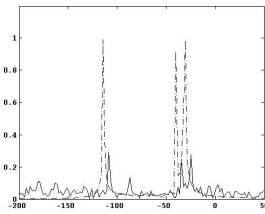
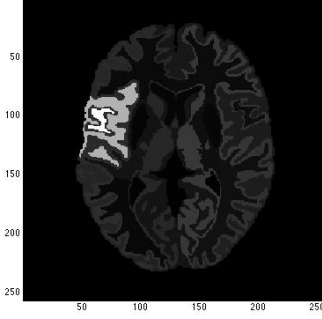
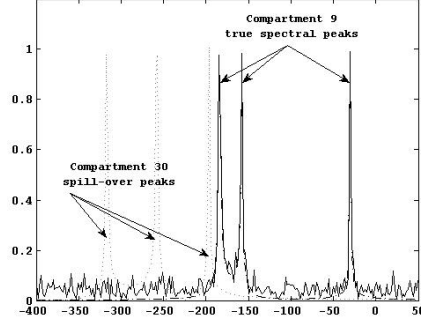


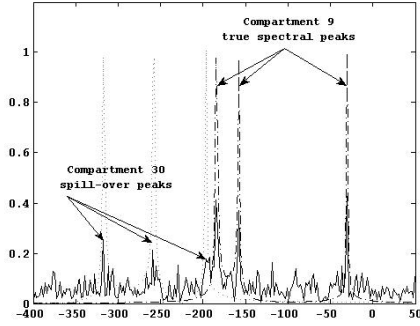
Figure 4.5: Spectra (continuous lines) resulting from the reconstruction of the noisy (15.7 dB SNR) data set, relating to compartments 9, 11 and 14. Despite the remarkable amount of noise added, the *starsSLIM* method still displays satisfactory matching of reconstructed spectral peaks with respect to both the simulated amplitude and frequency characteristic values. Again, and for each compartment, simulated and relative reconstructed spectra are displayed in the same plot.



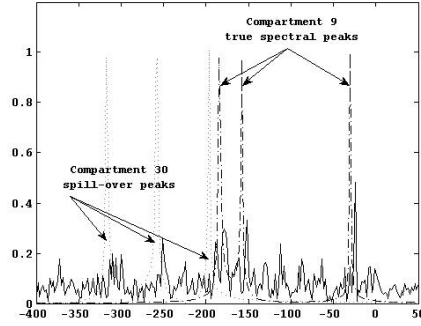
(a) Compartment 9 (white) and Compartment 30 (light gray).



(b) *star*SLIM.

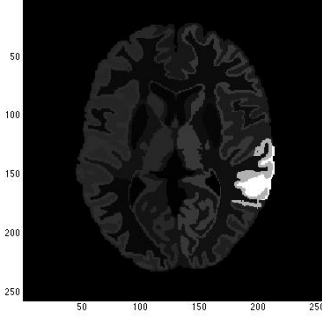


(c) BSLIM.

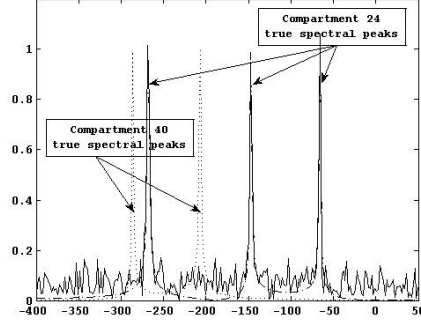


(d) SLIM.

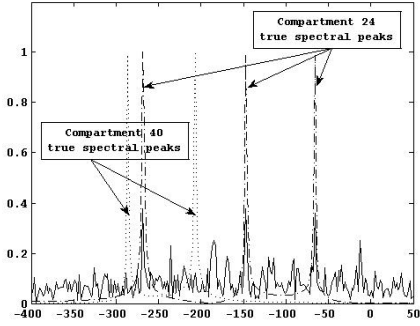
Figure 4.6: Reconstructed spectra from noisy k-space (continuous lines) relating to compartment 9. Plot 4.6b refers to the *star*SLIM method: no evidence of spillover peaks can be found. On the contrary, as seen with the noiseless raw data reconstruction, spectra from both the BSLIM and the SLIM method show the presence of spillover frequency peaks from compartment 30.



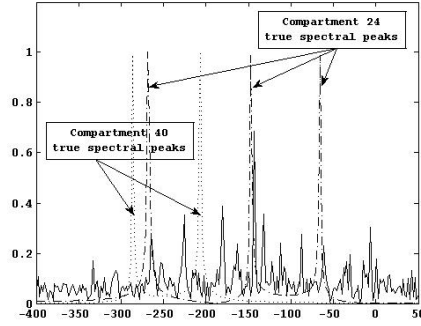
(a) Compartment 24 (white) and Compartment 40 (light gray).



(b) *starSLIM*.

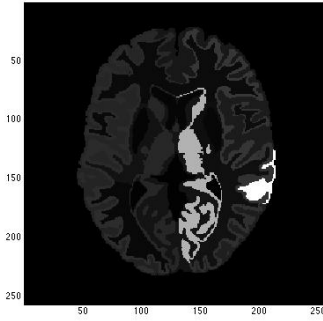


(c) BSLIM.

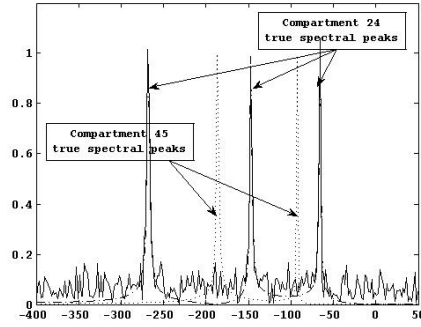


(d) SLIM.

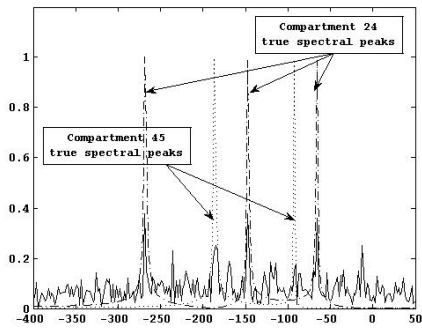
Figure 4.7: Reconstructed spectra from noisy k-space (continuous lines) relating to compartment 24. In spite of the noise, neither the plot 4.7b (displaying results from *starSLIM* method) nor the plots in 4.7c and 4.7d (BSLIM and SLIM methods, respectively) show evidence of spillover peaks from compartment 40. This may be due to the small size of compartment 40 with respect to compartment 24.



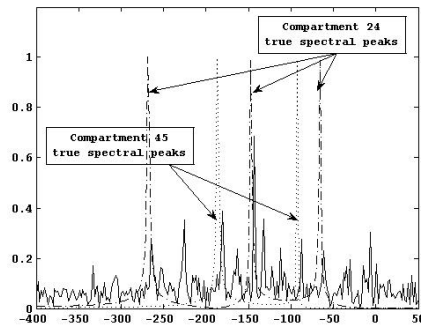
(a) *Compartment 24 (white) and Compartment 45 (light gray).*



(b) *starSLIM.*



(c) *BSLIM.*



(d) *SLIM.*

Figure 4.8: Reconstructed spectra from noisy k-space (continuous lines) relating to compartment 24. The comments reported in the legend to Fig.(4.4) remain valid in this case: a substantial spillover effect from compartment 45 is present in spectra from both the BSLIM and the SLIM method.